Visible Light-Induced Electron Transfer from Di-μ-oxo Bridged Dinuclear Mn Complexes to Cr Centers in Silica Nanopores

Walter W. Weare, Yulia Pushkar, Vittal K. Yachandra, and Heinz Frei*

Physical Biosciences Division, Lawrence Berkeley National Laboratory, University of California, Berkeley, CA 94720

Abstract

The compound $(bpy)_2Mn^{III}(\mu\text{-}O)_2Mn^{IV}(bpy)_2$, a structural model relevant for the photosynthetic water oxidation complex, was coupled to single Cr^{VI} charge-transfer chromophores in the channels of the nanoporous oxide AlMCM-41. Mn K-edge EXAFS spectroscopy confirmed that the di-μ-oxo dinuclear Mn core of the complex is unaffected when loaded into the nanoscale pores. Observation of the 16-line EPR signal characteristic of $Mn^{III}(\mu\text{-}O)_2Mn^{IV}$ demonstrates that the majority of the loaded complexes retained their nascent oxidation state in the presence or absence of Cr^{VI} centers. The FT-Raman spectrum upon visible light excitation of the $Cr^{VI}\text{-}O^{II} \rightarrow Cr^{V}\text{-}O^{I}$ ligand-to-metal charge-transfer reveals electron transfer from $Mn^{III}(\mu\text{-}O)_2Mn^{IV}$ (Mn-O stretch at 700 cm^{-1}) to Cr^{VI}, resulting in the formation of Cr^{V} and $Mn^{IV}(\mu\text{-}O)_2Mn^{IV}$ (Mn-O stretch at 645 cm^{-1}). All initial and final states are directly observed by FT-Raman or EPR spectroscopy, and the assignments corroborated by X-ray absorption spectroscopy measurements. The endoergic charge separation products (ΔE_o = -0.6 V) remain after several minutes, which points to spatial separation of Cr^{V} and $Mn^{IV}(\mu\text{-}O)_2Mn^{IV}$ as a consequence of hole (O^{I}) hopping as a major contributing mechanism. This is the first observation of visible light-induced oxidation of a potential water oxidation complex by a metal charge-transfer pump in a nanoporous environment. These findings will allow for the assembly and photochemical characterization of well defined transition metal molecular units, with the ultimate goal of performing endothermic, multi-electron transformations that are coupled to visible light electron pumps in nanostructured scaffolds.

1. Introduction

Synthetic polynuclear manganese complexes have received much attention as candidates for water oxidation catalysts in engineered solar to chemical conversion systems due to the role of Mn in the water oxidation complex of Photosystem II.[1] While only a few dinuclear Mn complexes have been implicated in the evolution of O_2 when chemically driven by strong oxidants in solution[2,3,4] or adsorbed on high surface area supports such as clays[4,5,6] or nanoporous silica[7], the vast majority of such polynuclear Mn compounds have served as structural models for the natural water oxidation complex.[8,9,10,11,12] These complexes are also useful for the study of electron transfer between a Mn core and an electron acceptor. Understanding the photon-driven electron transfer in all such systems has proven essential for the continued development of artificial photosynthetic systems.[13,14] For Mn based systems, Magnuson *et al.* and Burdinski *et al.* have demonstrated photon-induced electron transfer from a dinuclear Mn complex to a covalently attached $Ru(bpy)_3$; the latter functions as a charge-transfer pump by generating a transient Ru^{III} upon excitation of Ru^{II} in the presence of an acceptor in solution.[15,16,17] Synthetic manipulation of the chemical nature, the mode of attachment and the redox properties of the organic linkage between the Mn core and the Ru chromophore coupled with time-resolved optical spectroscopy of the systems has provided critical insights into the energetics and kinetics of sequential light-driven transfer of electrons out of the Mn core. In such systems, as many as three sequential oxidation steps are observed, with $Mn^{III}Mn^{IV}$ being the highest oxidation state achieved for the Mn core to date.[18] Knowledge of these physico-chemical properties are key for optimizing the efficiency for visible light-driven water oxidation catalysis.

Inorganic molecular photocatalytic units that are arranged and coupled on inert nanoporous oxide supports offer opportunities for developing artificial systems for sunlight to chemical energy conversion. Our approach features photocatalytic units consisting of a single metal center or an oxo-bridged heterobinuclear charge-transfer group that absorbs visible light to generate transient oxidizing (or reducing) intermediates. These can then be linked to multi-electron catalysts to achieve the desired reactivity. The photocatalytic units are covalently anchored on the surface of nanoporous silica materials, like MCM-41.[19,20,21,22,23] Such high surface area oxide supports allow for a high density of reactive sites while retaining the independence of each site as unique chemical species. The nanostructured features also offer possibilities to arrange and couple photocatalytic oxidation and reduction sites in ways that instantly separate the redox products, minimizing back reactions. The modular nature of such a system's polynuclear metal centers allows for optimization of several critical properties. These include redox level matches, visible light absorption characteristics, and efficient electronic coupling. We believe that the flexibility of this approach will eventually allow for the development of integrated sunlight to fuel conversion systems where each component is coupled to another with minimal loss of energy or charge.

In recent work, we demonstrated visible light-induced oxidation of water using iridium oxide (IrO_x) nanoclusters coupled to single Cr^{VI} or $TiOCr^{III}$ charge-transfer pumps in MCM-41 silica nanopores.[21,24] While this noble metal catalyst successfully oxidizes water, there is an urgent need for exploring Mn or other first row transition metal-based water oxidation catalysts because large scale deployment of solar fuel conversion systems requires the use of inexpensive, abundant materials. Equally

important, from a fundamental research standpoint, is the need to gain a detailed understanding of photon induced charge transfer processes between catalysts and visible light chromophores. Polynuclear transition metal complexes, as well-characterized molecular units, offer spectroscopic precision into chemical and electronic states at a level not readily attainable with metal oxide nanocluster catalysts.

In this paper, we report the coupling of molecular, bridging di-μ-oxo dinuclear Mn model catalysts, in particular $(bpy)_2Mn^{III}(\mu\text{-}O)_2Mn^{IV}(bpy)_2$, to single Cr^{VI} charge-transfer pumps loaded inside the nanopores of the silica material AlMCM-41. Visible light-driven transfer of electrons from the Mn core to the chromophore is demonstrated, with the core reaching its highest, $Mn^{IV}(\mu\text{-}O)_2Mn^{IV}$ oxidation state (Figure 1).

2. Results and Discussion

In the first part of this study, we focus on the structure and integrity of di-μ-oxo dinuclear Mn complexes upon loading into a nanoporous support (AlMCM-41, an aluminum functionalized amorphous silica material with 30 Å cylindrical channels and a surface area of 1250 m^2/g).[25] This is followed by experiments demonstrating that visible light drives the oxidation of the Mn core when coupled to a Cr^{VI} chromophore.

2.1 Characterization of $(bpy)_2Mn^{III}(\mu\text{-}O)_2Mn^{IV}(bpy)_2$ Loaded into Nanoporous Solid

Figure 2(I) shows the Fourier Transform (FT) of the Mn K-edge EXAFS of $(bpy)_2Mn^{III}(\mu\text{-}O)_2Mn^{IV}(bpy)_2$ loaded into Cr-AlMCM-41 (Cr/Si = 0.007 according to ICP/MS) (trace C) and plain AlMCM-41 (trace B). The loading level of the complex is

0.5 wt% (corresponding to a Cr:Mn_2 ratio of 11:1). For comparison, the FT of crystalline $[(bpy)_2Mn^{III}(\mu\text{-}O)_2Mn^{IV}(bpy)_2](NO_3)_3$ is included as trace A of Figure 2(I). The results of Mn K-edge EXAFS curve fitting for the three samples are summarized in Table 1. No significant differences are found for the Mn-O and Mn-N distances (first FT peak of Figure 2(I)) as well as the Mn-Mn distance (second FT peak) for the complex inside Cr-AlMCM-41, AlMCM-41, or in crystalline form. Also, the coordination numbers of the three samples agree within uncertainties. The intense Mn-Mn FT peak of trace B and C clearly demonstrates that the majority of the complexes have intact di-μ-oxo Mn dinuclear cores inside the silica nanopores in the presence or absence of Cr centers (at twenty-fold higher concentration of the complex, curve fitting gives a second Mn-Mn distance of 2.98 Å, probably due to Mn cluster formation. Corresponding Mn K-edge EXAFS curve fitting results are presented in Table S1 of the Supporting Information). The Mn K-edge XANES spectra of loaded $(bpy)_2Mn^{III}(\mu\text{-}O)_2Mn^{IV}(bpy)_2$ are similar to those of the reference compounds (Figure 2(II)) and changes very little between AlMCM-41 and Cr-AlMCM-41. One noticeable effect is the broadening of the shoulder on the rising edge at ~6555 eV, which has previously been assigned to a Mn to ligand π* transition.[26] This broadening implies that the bipyridine ligands become disordered when the dinuclear Mn complexes are adsorbed onto the surface, but the complex is otherwise intact. EPR spectra confirm that no breakup of the dinuclear Mn core takes place upon loading onto the silica support. The $Mn^{III}(\mu\text{-oxo})_2Mn^{IV}$ oxidation state is manifested in the EPR spectrum by a characteristic 16-line signal, shown in Figure 3.[28] This signal does not significantly change when the complex is loaded into nanoporous silica, as described in more detail below.

The ability of EPR spectroscopy to detect changes in $Mn^{III}(\mu\text{-}O)_2Mn^{IV}$ structure on the surface allows us to determine the longer term stability of the complex loaded into AlMCM-41. As seen in Figure 4, we are able to observe the formation of Mn^{II} from $Mn^{III}(\mu\text{-}O)_2Mn^{IV}$ over time, indicated by the appearance of its characteristic 6-line EPR signal. In the case of (terpy)$Mn^{III}(\mu\text{-}O)_2Mn^{IV}$(terpy), this reaction (presumably disproportionation) is observable within hours of loading and is complete within a day when the sample is maintained under ambient conditions. When $(bpy)_2Mn^{III}(\mu\text{-}O)_2Mn^{IV}(bpy)_2$ or $(phen)_2Mn^{III}(\mu\text{-}O)_2Mn^{IV}(phen)_2$ are loaded, we find that they remain stable for significantly longer periods of time, the formation of Mn^{II} is only observable after 3 weeks and is complete after 2-3 months under identical conditions. This remarkable stability of $(bpy)_2Mn^{III}(\mu\text{-}O)_2Mn^{IV}(bpy)_2$ within AlMCM-41 enables the detailed study of this system.

The FT of the Cr K-edge EXAFS (Figure 5(I)) shows the short 1.64 Å Cr=O distance characteristic for tetrahedral Cr^{VI} centers anchored on the silica pore surface.[21] The Cr K-edge EXAFS curve fitting results are summarized in Table 2. The analysis reveals two peaks: One corresponds to the two Cr=O bonds, the other indicates a longer Cr-O bond around 1.9 A, [21,25] in agreement with the expected $(SiO)_2Cr(O)_2$ structure of the site. The absence of an additional separate peak at ~2 Å indicates that reduction of Cr^{VI} (to Cr^{V}) is insignificant under these conditions, [21] confirming that Cr^{VI} is the prevalent chromium species before and after loading of the dinuclear Mn complexes. This finding is consistent with Cr K-edge XANES (Figure 5(II)) which shows negligible effect on the intensity of the 1s-3d pre-edge peak of Cr^{VI} upon loading of the dinuclear Mn complex into Cr-AlMCM-41 (0.5 wt%); Figure 5(II), curve G shows the intense Cr

K-edge XANES pre-edge peak of tetrahedral Cr^{VI} centers anchored on the silica pore surface. The band is characteristic for tetrahedrally coordinated Cr^{VI}, but is absent for octahedral (centrosymmetric) Cr^{III} shown in curve D for the case of $Cr(NO_3)_3$, typical for such systems.[27] The Cr pre-edge peak intensity is decreased by at most 15 percent upon loading of the Mn complex (curve F) or bipyridyl ligand (curve E). Furthermore, no second nearest neighbor signal is observed in the FT of the Cr K-edge EXAFS (Figure 5(I)), indicating that the interaction of the Cr center with the Mn complex does not give rise to an ordered structure as one might expect for a covalent Cr-O-Mn linkage. The absence of second nearest neighbor peaks also rules out the presence of Cr oxide clusters in the Cr-AlMCM-41 samples as these would give rise to Cr-Cr peaks.

While the Mn K-edge EXAFS and XANES data indicate a high degree of conservation of the di-μ-oxo structure of the $Mn(\mu\text{-}O)_2Mn$ core upon loading of the complex onto the nanoporous silica support, the 16-line EPR signal allows us to evaluate the integrity of the $Mn^{III}Mn^{IV}$ oxidation state upon loading.[28] No shifts of the peak positions of the EPR hyperfine lines are noted for $(bpy)_2Mn^{III}(\mu\text{-}O)_2Mn^{IV}(bpy)_2$ in solution (Figure 3, trace C), in Cr-AlMCM-41 (trace B) or AlMCM-41 (trace A). This confirms that no significant structural changes of the $Mn^{III}Mn^{IV}$ core occur when loaded into the silica channels. Slight broadening of the hyperfine splitting is noted upon adsorption of the complex, reflecting both the increased disorder of the ligand environment (as observed by Mn K-edge XANES) and the increased anisotropy of the environment for complexes adsorbed on nanoporous surfaces.[29] Also, no effect of the Cr centers on the $Mn^{III}Mn^{IV}$ spectrum is detected. While the majority of the Cr centers in calcined Cr-AlMCM-41 (Cr/Si = 0.007) are Cr^{VI}, a small fraction of the centers are Cr^{V}

($g_{\perp}$= 1.977, $g_{\parallel}$= 1.890 in Figure 3 (inset) - the $g_{\parallel}$ signal is obscured by the Mn 16-line signal in all other spectra).[21] We have found that the Cr^{V} signal decreases linearly with increased loading of the dinuclear Mn complex, likely by spontaneous thermal oxidation of $Mn^{III}Mn^{IV}$ to $Mn^{IV}Mn^{IV}$ (Figure S1 of Supporting Information). This is corroborated by the blue shift of the Mn K-edge XANES of $(bpy)_2Mn^{III}(\mu\text{-}O)_2Mn^{IV}(bpy)_2$ in Cr-AlMCM-41 relative to AlMCM-41 (Figure 2(II), curves E and F); in higher oxidation states the Mn K-edge XANES shift to higher energy.[30] The observation is in agreement with the strong oxidizing power of Cr^{V} in solution (E_o of 1.34 V,[31] compared to 1.16 V for $(bpy)_2Mn^{III}(\mu\text{-}O)_2Mn^{IV}(bpy)_2$[32]). Note that, by contrast, Cr^{VI} (E_o = 0.55 V[31]) is unable to spontaneously oxidize the dinuclear Mn complex to the $Mn^{IV}Mn^{IV}$ state as seen in Scheme 1. Although the true potentials of these redox active molecules on silica surfaces is not known, the solution measurements do allow for a correct prediction of the reactivity between these complexes. The presence of residual Cr^{V} at low loading levels also supports the idea that the dinuclear Mn complexes have limited mobility on the surface of AlMCM-41, as Cr^{V} would otherwise be titrated by excess $Mn^{III}Mn^{IV}$. Aside from this small effect of residual Cr^{V} on $Mn^{III}Mn^{IV}$ upon loading, the EPR spectra show that the concentration of $Mn^{III}Mn^{IV}$ species increases linearly with the amount of $(bpy)_2Mn^{III}(\mu\text{-}O)_2Mn^{IV}(bpy)_2$ loaded into the nanoporous Cr-AlMCM-41 or AlMCM-41, up to the maximum loading (~ 9 wt%).

(1)

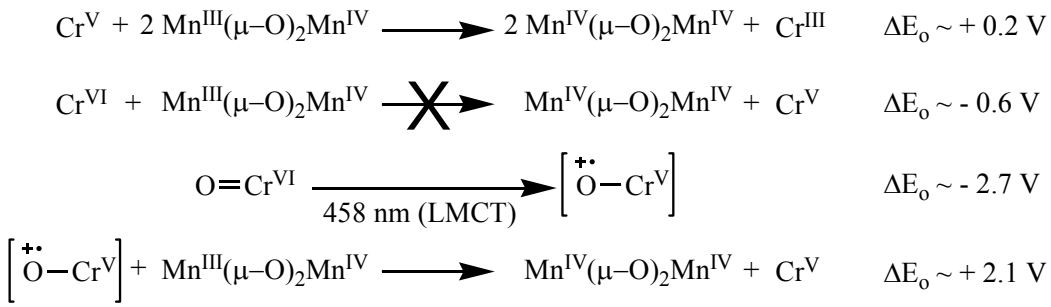

Scheme 1

The Mn-O stretch region of the FT-Raman spectrum allows us to simultaneously monitor the complex in the $Mn^{III}Mn^{IV}$ and the $Mn^{IV}Mn^{IV}$ oxidation state, in addition to observing possible effects of the loading on the bipyridyl ligand spectra. A comparison of spectra of the dinuclear Mn complex in Cr-AlMCM-41 at 2.5 % and 5 % loading is presented in Figure 6. Two bands show an approximate doubling of the intensity, namely one around 700 cm^{-1} and the other at 645 cm^{-1}. The 700 cm^{-1} feature is in the region where Mn-O modes of $Mn^{III}(\mu\text{-}O)_2Mn^{IV}$ are expected to absorb, while a band in the 640 – 650 cm^{-1} range is typical for Mn-O modes of $Mn^{IV}(\mu\text{-}O)_2Mn^{IV}$.[33] Based on this comparison to literature values, we assign the 700 cm^{-1} band to $Mn^{III}(\mu\text{-}O)_2Mn^{IV}$ and the absorption at 645 cm^{-1} to $Mn^{IV}(\mu\text{-}O)_2Mn^{IV}$. Note that the 700 cm^{-1} region is free of any absorption of bipyridyl (isolated or bound to Mn), while the 645 cm^{-1} band is overlapped by a broad ligand absorption (Figures S2 and S5). Hence, this pair of Raman bands, along with the Mn K-edge XANES results, allows us to qualitatively follow the relative abundance of oxidation states for the dinuclear Mn complex. Moreover, the 893 cm^{-1} band in the FT-Raman spectrum, originating from the symmetric $O{=}Cr^{VI}{=}O$ mode, allows us to simultaneously monitor the concentration of the Cr^{VI} species. Aside from these absorptions, all other bands in the FT-Raman spectrum are due to bipyridyl ligand

absorptions. While there are small differences of the ligand spectrum of the crystalline Mn complex compared to the spectrum of the loaded complex, no significant effect of the presence of Cr on band frequencies or intensities is observed. Since the ligand is in large molar excess of (bpy:Mn_2 = 25:1 in this system) this is to be expected.

In summary, the spectroscopic characterization of $(bpy)_2Mn^{III}(\mu\text{-}O)_2Mn^{IV}(bpy)_2$ loaded into the channels of Cr-AlMCM-41 sieve reveals a material with the structure of the Mn complex completely intact and the oxidation state largely retained, and with almost all Cr centers in the oxidation state Cr^{VI}. **The dominating driving force for adsorption of the Mn dimer complex into the silica nanopores are most probably dispersion interaction and H-bonding, especially between the bpy ligands and the siloxane and surface silanol groups as already evidenced by the ease of adsorption of free bpy ligands onto MCM-41.**

2.2 Light-driven Oxidation of $Mn^{III}Mn^{IV}$ to $Mn^{IV}Mn^{IV}$ by Cr^{VI} Ligand to Metal Charge Transfer (LMCT) Excitation

Upon illumination with visible light, samples of Cr-AlMCM-41 containing 1.5 wt % $(bpy)_2Mn^{III}(\mu\text{-}O)_2Mn^{IV}(bpy)_2$ were found to have undergone the redox reaction $Cr^{VI} + Mn^{III}Mn^{IV} \rightarrow Cr^{V} + Mn^{IV}Mn^{IV}$, which is endoergic by 0.61 V.[31,32] Each reactant and product redox state was observed upon illumination using a combination of EPR, XANES, and FT-Raman spectroscopy. As seen in Figure 7(I), the FT-Raman band of $(Mn^{III}(\mu\text{-}O)_2Mn^{IV})$ at 700 cm^{-1} decreases during illumination; spectra following 5 min (trace B) and 30 min (trace C) irradiation at 458 nm (170 mW) are shown - see Supporting Information (Figure S7) for the DRS of these materials.[23] Note that the

features around 700 cm^{-1} remaining after 30 min illumination are not noise but coincide with bands observed when $(bpy)_2Mn^{III}(\mu\text{-}O)_2Mn^{IV}(bpy)_2$ is loaded into AlMCM-41 at low concentration (0.5 wt% - trace D). This shows that the $Mn^{III}Mn^{IV}$ complexes remaining after continued illumination occupy similar sites to those preferentially occupied at low loading levels. No visible light-induced depletion is observed for the complex in AlMCM-41 (free of Cr), as shown in Figure 7(II). This excludes the possibility of $Mn^{III}Mn^{IV}$ depletion through light absorption by the dinuclear Mn complex itself. In agreement with the Raman observations, EPR spectroscopy shows a decrease in intensity for the 16-line signal of $Mn^{III}(\mu\text{-}O)_2Mn^{IV}$ for the complex loaded into Cr-AlMCM-41 (Figure 8, spectra A and B), but no change for the complex loaded into AlMCM-41 (Figure 8, spectra C and D). We conclude that $Mn^{III}(\mu\text{-}O)_2Mn^{IV}$ in Cr-AlMCM-41 is oxidized upon visible light excitation of the Cr^{VI} ligand-to-metal charge-transfer (LMCT) chromophore.

The product of this photooxidation is $Mn^{IV}(\mu\text{-}O)_2Mn^{IV}$, as indicated by the increase of the band at 645 cm^{-1} in the FT-Raman spectrum.[33] While bpy ligand bands also absorb in this region (see Figures S2 and S5 in Supporting Information), the increase in intensity upon illumination only occurs when both Cr^{VI} and $Mn^{III}(\mu\text{-}O)_2Mn^{IV}$ are present. Assignment of the photoproduct to $Mn^{IV}(\mu\text{-}O)_2Mn^{IV}$ is also supported by the observation that, upon disappearance of $Mn^{III}(\mu\text{-}O)_2Mn^{IV}$, no other EPR active Mn signal is observed. In particular, no Mn^{II}, a known disproportionation product of this type of complex[30] with its characteristic 6-line signal (Figure 4C), is formed. Since $Mn^{IV}(\mu\text{-}O)_2Mn^{IV}$ is EPR silent, the absence of additional Mn signals upon illumination is consistent with the formation of $Mn^{IV}(\mu\text{-}O)_2Mn^{IV}$. Furthermore, X-ray absorption spectra

of samples of the dinuclear Mn complex on Cr-AlMCM-41 recorded before and after illumination exhibit an ~ 1 eV shift of the Mn K-edge XANES 2nd derivative zero crossing point to higher energy (Figure 9(I)), which is characteristic for oxidation of the Mn center.[26]

The decrease of the Cr^{VI} Raman mode at 895 cm^{-1}, assigned to the symmetric Cr=O mode of tetrahedral Cr^{VI},[20] upon 458 nm irradiation (Figure 7(I)) and concurrent growth of the $g_{\perp}$ = 1.977 EPR signal of Cr^{V} (Figure 8B) confirms that photooxidation of $Mn^{III}(\mu\text{-}O)_2Mn^{IV}$ to Mn^{IV} $(\mu\text{-}O)_2Mn^{IV}$ is accompanied by the reduction of Cr^{VI} to Cr^{V} (see Scheme 1). The corresponding bands are absent when conducting the illumination with dinuclear Mn complexes loaded into AlMCM-41 (Figure 7(II) and Figure 8D). The reduction of the Cr centers is further confirmed by red shift of ~1 eV in the Cr K-edge XANES 2nd derivative zero crossing point,[27] as shown in Figure 9(II)). We conclude that photo-excitation of Cr^{VI}-O LMCT induces electron transfer from $Mn^{III}(\mu\text{-}O)_2Mn^{IV}$ to Cr^{VI}, resulting in the formation of $Mn^{IV}(\mu\text{-}O)_2Mn^{IV}$ and Cr^{V}.

Based on the number of photons absorbed by Cr^{VI} LMCT at 458 nm and the number of $Mn^{III}(\mu\text{-}O)_2Mn^{IV}$ complexes converted to $Mn^{IV}(\mu\text{-}O)_2Mn^{IV}$ as determined by the decrease in the intensity of the 16-line EPR signal, a quantum efficiency of 10 percent was estimated for the light-induced electron transfer (this constitutes a lower limit because it is assumed that each Cr^{VI} center in the silica material contributes to photon-induced electron transfer, which may not be the case). The estimate shows that the uphill electron transfer $Cr^{VI} + Mn_2^{III,IV} \rightarrow Cr^{V} + Mn_2^{IV,IV}$ with ΔE_o = - 0.61 V[31,32] results in a substantial fraction of the charge separated products surviving on the time scale of minutes at room temperature. To our knowledge, this is the first observation of visible

light-driven oxidation of a dinuclear Mn complex to the (IV,IV) oxidation state. The most likely origin of the long life time of the charge separated products is hole hopping on intervening oxygen atoms: upon activation of the Cr^{VI}-O ligand-to-metal charge-transfer state to yield Cr^{V}-O• (Scheme 1), the transient hole on O can hop to a neighboring O of the silica environment (i.e. Cr-O• to Si-O•) before pulling an electron from a $Mn^{III}(\mu\text{-}O)_2Mn^{IV}$ unit. For such a configuration, back electron transfer from Cr^{V} to the oxidized dinuclear Mn complex is expected to be slow due to the separation of the metal centers by Si-O-Si surface groups. This result also suggests that the dinuclear Mn complexes are effectively immobile on the nanopore surfaces. There is very likely a distribution of lifetimes for the charge separated products due to differences in the way dinuclear Mn complexes are arranged around Cr centers. Furthermore, a factor that may contribute to the very long-lived charge separation is the large reorganization energy associated with Cr^{VI} to Cr^{V} reduction (replacement of the short Cr=O double bond by the 0.4 A longer Cr-O single bond)[21], which will slow down back reaction. Time-resolved optical studies of electron transfer between the dinuclear Mn complex and the Cr^{VI} chromophore are needed to obtain a complete overview of the electron transfer processes and their kinetics. Such studies are in progress.

3. Conclusions

In summary, we have loaded transition metal di-μ-oxo dinuclear Mn complexes with bpy, phen, or terpy ligands into nanoporous silica materials. The complex with bpy ligands exhibited by far the best stability. FT-Raman, EXAFS, XANES, and EPR spectroscopy confirmed that $(bpy)_2Mn^{III}(\mu\text{-}O)_2Mn^{IV}(bpy)_2$ retains its structural integrity

inside the nanoscale silica channels for weeks at room temperature. Moreover, the majority of the $(bpy)_2Mn(\mu\text{-}O)_2Mn(bpy)_2$ complexes remain in the (III,IV) oxidation state upon loading; no Mn^{II} containing decomposition products were observed. Excitation of the Cr^{VI}-O LMCT absorption with visible light results in the oxidation of the dinuclear Mn(III,IV) state to Mn_2O_2(IV,IV), with all initial and final states of the electron transfer spectroscopically identified. The charge separation products were found to last up to several minutes at room temperature. Charge transport from the Cr-O sites to the dinuclear Mn complexes by hole hopping is thought to be primarily responsible for the long lifetime of the charge separation because it allows for significant spatial separation of the Cr and Mn centers.

With this direct spectroscopic observation of visible light-driven oxidation of a complex relevant to water oxidation by a metal center chromophore in silica nanopores, we are able to begin studying the detailed energetics and kinetics of photon-induced electron flow between multi-electron transfer catalysts and a molecular charge-transfer chromophores inside high-surface area oxide supports. A complete assessment of the electron transfer processes of the photocatalytic units requires time-resolved monitoring of the various spectra, which will become particularly important as the single Cr LMCT center is replaced by a heterodinuclear charge-transfer chromophore with a donor potential that can be tuned or selected.[21]

Acknowledgment

This work was supported by the Director, Office of Science, Office of Basic Energy Sciences, Division of Chemical Sciences, Geosciences and Biosciences of the

U.S. Department of Energy under Contract DE-AC02-05CH11231. Portions of this research were carried out at the Stanford Synchrotron Radiation Laboratory, a national user facility operated by Stanford University on behalf of the U.S. Department of Energy, Office of Basic Energy Sciences. The SSRL Structural Molecular Biology Program is supported by the Department of Energy, Office of Biological and Environmental Research, and by the National Institutes of Health, National Center for Research Resources, Biomedical Technology Program. We thank Dr. Junko Yano (LBNL) for discussions regarding the analysis and interpretation of the EPR and X-ray spectroscopy data and for her contributions to the collection of these data. The compound $(Me_2\text{-}bpy)_2Mn^{IV}(\mu\text{-}O)_2Mn^{IV}(Me_2bpy)_2$ was provided by William Armstrong and Sumitra Mukerji (BCC).

Experimental

Unless otherwise noted, all manipulations were carried out under ambient conditions with solvents and materials used as received from the manufacturer.

Synthesis of di-μ-oxo dinuclear Mn complexes $[bpy_4Mn_2(\mu\text{-}O)_2][BF_4]_3$,[34] $[phen_4Mn_2(\mu\text{-}O)_2][BF_4]_3$,[35] and $[terpy_2Mn_2(\mu\text{-}O)_2\ (H_2O)_2][NO_3]_3$,[36,37] were synthesized by literature methods or small variations thereof.

Synthesis of Cr-AlMCM-41 and AlMCM-41 Cr-AlMCM-41 was synthesized via hydrothermal synthesis as previously described.[24] Briefly, a solution of diethylamine (10 mL), 25 wt% cetyl trimethylammonium chloride (7.2 mL) and $Al(NO_3)_2 \bullet 9H_2O$ (0.6 g) in H_2O (65 mL) was prepared. A separate solution of $Cr(NO_3)_3 \bullet 9H_2O$ (0.065 g) in 25 wt% NH_4OH (3.6 mL) was sonicated for 30 minutes. The two solutions are combined

and stirred for 30 minutes. Then, tetraethylorthosilicate (8.9 mL) is added dropwise, resulting in a white slurry that is stirred for 4 hours. This mixture is transferred into a Parr bomb, sealed, and heated at 110 °C for 3 days. The resulting light blue solid is collected via filtration, washed with copious amounts of water, and dried at 100 °C for 6 hours. This is followed by calcination at 630 °C for 6 hours under air flow (1 °C per minute ramp), resulting in a light yellow product. EPR spectroscopy revealed residual Cr^{V} not exceeding 5 percent (Reference 21, Figure 4A, spectrum a). These centers are most likely in the interior of the silica walls separating the nanoscale channels and, hence, not reachable by oxygen. AlMCM-41 is synthesized by omitting $Cr(NO_3)_3$ from the above preparation. These materials were identical by IR, FT-Raman, and DRS to samples previously prepared in our laboratory.[24]

Grafting $bpy_4Mn_2(\mu\text{-}O)_2$ into AlMCM-41 AlMCM-41 (100 mg) was placed in 10 mL of acetonitrile buffered with 0.01 M 2,2'-bipyridine (0.01 M bpy buffer) with vigorous stirring to form a slurry. Separately, a stock solution containing 1 mM (~ 1 mg/mL) of $[bpy_4Mn_2(\mu\text{-}O)_2][BF_4]_3$ in 0.01 M bpy buffer was prepared. The buffer is necessary as, according to our experience, $[bpy_4Mn_2(\mu\text{-}O)_2][BF_4]_3$ slowly decomposes to form a brown solid in pure acetonitrile.[32]

Depending on the amount of $bpy_4Mn_2(\mu\text{-}O)_2$ loaded in the material, an appropriate amount of the stock solution is added dropwise into the AlMCM-41 slurry and allowed to stir for one hour. Then, the solid is filtered, washed with 5 x 20 mL acetonitrile, and dried *in vacuo* for 2 hours. The final solid typically has no residual CH_3CN by FT-Raman and FT-IR. These materials are characterized by FT-Raman, EPR,

TGA, DRS, and ICP-MS. Identical procedures are used to graft $bpy_4Mn_2(\mu\text{-}O)_2$ into Cr-AlMCM-41.

Grafting $phen_4Mn_2(\mu\text{-}O)_2$ into AlMCM-41 Samples are prepared similarly to $bpy_4Mn_2O_2$ grafted materials, substituting $[phen_4Mn_2(\mu\text{-}O)_2][BF_4]_3$ and 0.01 M 1,10-phenanthroline in acetonitrile (0.01 M phen buffer). These materials are characterized by EPR and FT-Raman. Although EPR demonstrates that $Mn^{III}(\mu\text{-}O)_2Mn^{IV}$ is grafted, we were unable to identify a strong characteristic FT-Raman signal for further study. This is due to ligand bands that overlap the area of interest. See Supporting Information for further characterization of this material (Figures S17 and S18).

Grafting $terpy_2Mn_2(\mu\text{-}O)_2$ into AlMCM-41 The samples were manipulated similarly to other materials of this type. The grafting solution was prepared from a methanol solution of $[terpy_2Mn_2(\mu\text{-}O)_2][NO_3]_3$ (1 mM) and an appropriate amount added to a separate slurry of 100 mg of AlMCM-41 in 10 mL of methanol and stirred for one hour. The resulting solid was filtered, washed with methanol (5 x 20 mL), and dried *in vacuo*. The material was characterized by EPR and FT-Raman. While EPR of immediately frozen (liq. N_2) materials showed that $Mn^{III}(\mu\text{-}O)_2Mn^{IV}$ is successfully grafted into AlMCM-41, no strong characteristic FT-Raman signals could be observed for $Mn^{III}(\mu\text{-}O)_2Mn^{IV}$. This could be due to the instability of $terpy_2Mn_2^{III/IV}O_2$ within AlMCM-41 (Figure 4) or overlapping ligand absorptions in the region of interest. See Supporting Information for more details of this material (Figure S16).

Determining maximum load of $L_4Mn_2(\mu\text{-}O)_2$ into AlMCM-41 A 1 mM solution of $[L_4Mn_2(\mu\text{-}O)_2][BF_4]_3$ (L=bpy, phen) in 0.01 M L acetonitrile was prepared. This is then added in differing amounts to approximately 30 mg of AlMCM-41, resulting in final

loading levels between 10 and 15 wt%. For instance, 3.5 mL of a 1 mM stock solution is added to 27.8 mg of AlMCM-41, resulting in a maximum possible load of 12.3 wt%. This solution is stirred for 1 hour and then filtered to collect the supernatant. The supernatant is compared to the remaining stock solution by UV/Vis spectroscopy. The amount of $[L_4Mn_2(\mu\text{-}O)_2][BF_4]_3$ remaining in solution after grafting was measured by comparing four points (450 nm, 530 nm, 600 nm, 690 nm) before and after the grafting procedure. Each material combination was measured at three loading levels (typically 10, 12 and 15 wt%), with the results combined to provide the values shown in Table S2 in the Supporting Information. The $bpy_4Mn_2(\mu\text{-}O)_2$ system has slightly higher maximum loading than $phen_4Mn_2(\mu\text{-}O)_2$ (~ 9:7.5 wt%). There was no significant difference between loading on AlMCM-41 and Cr-AlMCM-41 in either system.

FT-Raman sample preparation and data acquisition Samples were prepared by pressing approximately 1 mg of material into an aluminum sample well. Spectra were collected on a Bruker model IFS66 spectrometer with a FT-Raman module FRA-106 fitted with a liquid N_2-cooled Ge detector. Samples were typically illuminated with 1064 nm laser probe light at 300 mW, with 1000 scans recorded per sample.

EPR analysis of Mn containing Cr-AlMCM-41 and AlMCM-41

X-band EPR spectroscopy was performed with a Varian E-109 spectrometer, a standard TE_{102} cavity, and an Air Products liquid helium cryostat. EPR spectra were typically collected at 20 K using 1 mW microwave power and 32 G modulation amplitude. Samples are prepared by lightly crushing the material, followed by placing it into a tared quartz EPR tube which is then sealed.

EXAFS data collection X-ray absorption spectra were collected at the Stanford Synchrotron Radiation Laboratory (SSRL) on beamline 7-3 at electron energy 3.0 GeV and an average current 100-500 mA. The beamline is equipped with a Si(220) double crystal monochromator. The intensity of the incident X-rays was monitored by a N_2-filled ion chamber (I_0) in front of the sample. To reduce the sample damage by radiation, the incident X-ray beam was defocused at the sample position. The samples were protected from the beam during spectrometer movements between different energy positions by a shutter synchronized with the scan program. The samples were kept at 9 ± 1 K in a He atmosphere at ambient pressure using an Oxford CF-1208 continuous-flow liquid He cryostat. Data were recorded as fluorescence excitation spectra using a germanium 30-element energy-resolving detector (Canberra Electronics). For Mn K-edge XAS, energy was calibrated by the pre-edge peak of $KMnO_4$ (6543.3 eV), which was placed between two N_2-filled ionization chambers (I_1 and I_2) after the sample. For Cr K-edge XAS, Cr foil was used with (E_0=5989.0 eV) corresponding to the first peak of the first derivative on the Cr^0 edge.

EXAFS data analysis Data reduction has been described previously[38] and is described in more details in the Supporting Information (Figures S3 and S4).

Stability of grafted $L_xMn_2(\mu\text{-}O)_2$ AlMCM-41 materials Samples were stored under air at room temperature and periodically removed for EPR and FT-Raman analysis. In the case of $terpy_2Mn_2O_2$ grafted materials, the initial samples were immediately frozen under liquid nitrogen after the grafting procedure was completed for EPR and FT-Raman analysis. It was found that $L_4Mn_2(\mu\text{-}O)_2$ (L=bpy, phen) were stable for weeks to months under ambient conditions, while $terpy_2Mn_2(\mu\text{-}O)_2$ samples were stable for only a few

hours, forming unidentified Mn^{II} products (see Figure 4). EPR shows that a similar Mn^{II} product is the final result for all AlMCM-41 material containing $L_xMn_2(\mu\text{-}O)_2$ cores.

Illumination of Cr-AlMCM-41 and AlMCM-41 containing $bpy_4Mn_2(\mu\text{-}O)_2$ Samples were prepared by pressing ~ 5 mg of material into a pellet 1 cm in diameter using 2 tons of force. The pellet was placed in a stainless steel IR vacuum cell equipped with CaF_2 or KBr windows. Samples in the evacuated cell are illuminated with 458 nm Ar ion laser emission at 170 mW, with the beam expanded to 1 cm to cover the entire sample pellet. At time intervals between 0 (control) and 30 minutes samples are removed from the beam for analysis by FT-Raman or EPR. For EPR measurements, the pellet was crushed, placed in quartz EPR tubes, and stored under liquid N_2 if there was a time lag between illumination and recording of spectra.

References

[1] Yano, J.; Kern, J.; Sauer, K.; Latimer, M.J.; Pushkar, Y.; Biesiadka, J.; Loll, B.; Saenger, W.; Messinger, J.; Zouni, A.; Yachandra, V.K. *Science* **2006**, *314*, 821-825.

[2] Chen, H.; Tagore, R.; Das, S.; Incarvito, C.; Faller, J.W.; Crabtree, R.H.; Brudvig, G.W. *Inorg. Chem.* **2005**, *44*, 7661-7670.

[3] Chen, H.; Tagore, R.; Olack, G.; Vrettos, J.S.; Weng, T.C.; Penner-Hahn, J.; Crabtree, R.H.; Brudvig, G.W. *Inorg. Chem.* **2007**, *46*, 34-43.

[4] Yagi, M.; Kaneko, M. *Chem. Rev.* **2001**, *101*, 21-35.

[5] Yagi, M.; Narita, K. *J. Am. Chem. Soc.* **2004**, *126*, 8084-8085.

[6] Narita, K.; Kuwabara, T.; Sone, K.; Shimizu, K.; Yagi, M. *J. Phys. Chem. B* **2006**, *110*, 23107-23114.

[7] Rumberger, E.M.W.; Bell, A.T., Tilley, T.D. 233rd ACS National Meeting, Symposium on Catalysis Relevant to Energy and Sustainability; Chicago, March, 2007.

[8] Ruettinger, W.; Dismukes, G.C. *Chem. Rev.* **1997**, *97*, 1-24.

[9] Manchanda, R.; Brudvig, G.W.; Crabtree, R.H. *Coord. Chem. Rev.* **1995**, *144*, 1-38.

[10] Pecoraro, V.L.; Baldwin, M.J.; Gelasco, A. *Chem. Rev.* **1994**, *94*, 807-826.

[11] Law, N.A.; Caudle, M.T.; Pecoraro, V.L. In *Advances in Inorganic Chemistry;* Academic Press: San Diego, 1999; Vol. 46.

[12] Mukhopadhyar, S.; Mandal, S.K.; Beaduri, S.; Armstrong, W.H. *Chem. Rev.* **2004**, *104*, 3981-4026.

[13] Gust, D.; Moore, T. A.; Moore, A. L. *Acc. Chem. Res*. **2001**, *34*, 40-48.

[14] Morris, N. D.; Suzuki, M.; Mallouk, T. E. *J. Phys. Chem. A*. **2004**, *108*, 9115-9119.

[15] Sun, L.C.; Raymond, M.K.; Magnuson, A.; LeGourrierec, D.; Tamm, M.; Abrahamsson, M.; Kenez, P.H.; Martensson, J.; Stenhagen, G.; Hammarstrom, L.; Styring, S.; Akermark, B.; *J. Inorg. Biochem.* **2000**, *78*, 15-22.

[16] Borgstrom, M.; Shaikh, N.; Johansson, O.; Anderlund, M.F.; Styring, S.; Akermark, B.; Magnuson, A.; Hammarstrom, L. *J. Am. Chem. Soc.* **2005**, *127*, 17504-17515.

[17] Burdinski, D.; Wieghardt, K.; Steenken, S. *J. Am. Chem. Soc.* **1999**, *121*, 10781-10787.

[18] Huang, P.; Magnuson, A.; Lomoth, R.; Abrahamsson, M.; Tamm, M.; Sun, L.; van Rotterdam, B.; Park, J.; Hammarstrom, L.; Akermark, B.; Styring, S. *J. Inorg. Biochem.* **2002**, *91*, 159-172.

[19] Lin, W.; Frei, H. *J. Phys. Chem. B* **2005**, *109*, 4929-4935.

[20] Lin, W.; Frei, H. *J. Am. Chem. Soc.* **2005**, *127*, 1610-1611.

[21] Han, H.; Frei, H., *J. Phys. Chem. C* **2008**, *112*, 000.

[22] Wu, X.; Han, H.; Frei, H., *manuscript in preparation*.

[23] Nakamura, R.; Okamoto, A.; Osawa, H.; Irie, H.; Hashimoto, K. *J. Am. Chem. Soc.* **2007**, *129*, 9596.

[24] Nakamura, R.; Frei, H. *J. Am. Chem. Soc.* **2006,** *128*, 10668-10669.

[25] Weckhuysen, B. M.; Wachs, I. E.; Schoonheydt, R. A**.** *Chem. Rev.* **1996,** *96*, 3327-3350.

[26] Visser, H.; Anxolabehere-Mallart, E.; Bergmann, U.; Glatzel, P.; Robblee, J. H.; Cramer, S. P.; Girerd, J.-J.; Sauer, K.; Klein, M. P.; Yachandra, V. K. *J. Am. Chem. Soc.* **2001**, *123*, 7031-7039.

[27] Bajt, S.; Clark, S. B.; Sutton, S. R.; Rivers, M. L.; Smith, J. V. *Anal. Chem.* **1993**, *65*, 1800-1804.

[28] Cooper, S. R.; Dismukes, G. C.; Klein, M. P.; Calvin, M. *J. Am. Chem. Soc.* **1978**, *100*, 7248-7252.

[29] Lunina, E.V. *Appl. Spectrosc.* **1996**, *50*, 1413-1420

[30] Yachandra, V. K.; Sauer, K.; Klein, M. P. *Chem. Rev*. **1996**, *96*, 2927-2950.

[31] Bard, A.J., Parsons, R., Jordan, J., Eds. *Standard Potentials in Aqueous Solution*; Marcel Dekker Inc.: New York, NY, 1985.

[32] Collomb Dunand-Sauthier, M-N.; Deronzier, A.; Pradon, X.; Ménage, S.; Philouze, C. *J. Am. Chem. Soc.* **1997**, *119*, 3173-3174.

[33] Hasegawa, K.; Ono, T. *Bull. Chem. Soc. Jpn.* **2006**, *79*, 1025-1031.

[34] Cooper, S.R.; Calvin, M. *J. Am. Chem. Soc.* **1977**, *99*, 6623-6630. $NaBF_4$ is substituted for $NaClO_4$ in the synthesis.

[35] Morrison, M.M.; Sawyer, D.T. *J. Am. Chem. Soc.*, **1977**, *99*, 257-258. $NaBF_4$ is substituted for $NaClO_4$ in the synthesis.

[36] Limburg, J.; Vrettos, J.S.; Liable-Sands, L.M. Rheingold, A.L.; Crabtree, R.H.; Brudvig, G.W. *Science* **1999**, *283*, 1524-1527.

[37] Collomb, M-N.; Deronzier, A.; Richardot, A.; Décant, J. *New J. Chem.* **1999**, *23*, 351-353.

[38] Robblee, J. H.; Messinger, J.; Cinco, R. M.; McFarlane, K. L.; Fernandez, C.; Pizarro, S. A.; Sauer, K.; Yachandra, V. K. *J. Am. Chem. Soc.* **2002**, *124*, 7459-7471.

Figure Captions

Table 1: Mn K-edge EXAFS curve fitting results for $(bpy)_2Mn^{III}(\mu\text{-}O)_2Mn^{IV}(bpy)_2$ loaded into AlMCM-41, Cr-AlMCM-41, and for crystalline $[(bpy)_2Mn^{III}(\mu\text{-}O)_2Mn^{IV}(bpy)_2](NO_3)_3$. Asterisk denotes values that were fixed during minimization.

Table 2: Cr K-edge EXAFS curve fitting results for Cr-AlMCM-41, 0.5 wt% $(bpy)_2Mn^{III}(\mu\text{-}O)_2Mn^{IV}(bpy)_2$ loaded into Cr-AlMCM-41, and 9.0 wt%$(bpy)_2Mn^{III}(\mu\text{-}O)_2Mn^{IV}(bpy)_2$ loaded into Cr-AlMCM-41. Asterisk denotes values that were fixed during minimization.

Figure 1: A schematic representation of the photon-induced electron transfer reaction. Light excites a Cr^{VI}-O LMCT, creating the high energy intermediate that transfers an electron from $(bpy)_2Mn^{III}(\mu\text{-}O)_2Mn^{IV}(bpy)_2$ into Cr^{VI}, creating Cr^{V}.

Figure 2: (I) FT of the k^3-weighted Mn K-edge EXAFS of (A) crystalline $[(bpy)_2Mn^{III}(\mu\text{-}O)_2Mn^{IV}(bpy)_2](NO_3)_3$. (B) $(bpy)_2Mn^{III}(\mu\text{-}O)_2Mn^{IV}(bpy)_2$ loaded (0.5 wt%) into AlMCM-41. (C) Complex loaded into Cr-AlMCM-41 (Cr/Si = 0.01). (II) Mn K-edge XANES of (D) crystalline $[(bpy)_2Mn^{III}(\mu\text{-}O)_2Mn^{IV}(bpy)_2](NO_3)_3$. $(bpy)_2Mn^{III}(\mu\text{-}O)_2Mn^{IV}(bpy)_2$ loaded into (E) AlMCM-41 (0.5 wt%), (F) complex loaded into Cr-

AlMCM-41. (G) Crystalline $[(Me_2\text{-bpy})_2Mn^{IV}(\mu\text{-}O)_2Mn^{IV}(Me_2\text{-bpy})_2][ClO_4]_4$. D and G are included to reference the edge position of $Mn_2^{III/IV}$ and $Mn_2^{IV/IV}$, respectively.

Figure 3: X-band EPR spectra of $(bpy)_2Mn^{III}(\mu\text{-}O)_2Mn^{IV}(bpy)_2$ grafted into (A) AlMCM-41, (B) Cr-AlMCM-41. (C) $[(bpy)_2Mn^{III}(\mu\text{-}O)_2Mn^{IV}(bpy)_2](NO_3)_3$ in acetonitrile solution. Spectra were recorded at 20 K. The small signal at ~3300 G originates from the residual Cr^V present in Cr-AlMCM-41. Inset is an EPR spectrum of calcined Cr-AlMCM-41 for comparison.

Figure 4: X-band EPR signal of AlMCM-41 grafted with 4 wt% $terpy_2Mn_2O_2$. The samples were kept under ambient conditions for (A) 10 minutes, (B) 6 hours, and (C) 7 days after grafting was complete, then frozen under liquid N_2 for EPR analysis. EPR intensities were arbitrarily normalized for comparison.

Figure 5: (I) FT of k^3-weighted Cr K-Edge EXAFS of (A) Cr-AlMCM-41, (B) Cr-AlMCM-41 grafted with 9.5 wt% $(bpy)_2Mn^{III}(\mu\text{-}O)_2Mn^{IV}(bpy)_2$, (C) Cr-AlMCM-41 grafted with 0.5 wt% $(bpy)_2Mn^{III}(\mu\text{-}O)_2Mn^{IV}(bpy)_2$. (II) Cr K-edge XANES of (D) $Cr(NO_3)_3$ (solid Cr(III) compound), (E) Cr-AlMCM-41 treated with 0.01 M 4,4'-bipyridine, (F) Cr-AlMCM-41 grafted with 0.5 wt% $(bpy)_2Mn^{III}(\mu\text{-}O)_2Mn^{IV}(bpy)_2$, (G) calcined Cr-AlMCM-41.

Figure 6: FT-Raman of $(bpy)_2Mn^{III}(\mu\text{-}O)_2Mn^{IV}(bpy)_2$ grafted onto Cr-AlMCM-41 in different weight ratios: (A) 2.5 wt%, (B) 5.0 wt%. Spectra are normalized relative to the bipyridyl ligand absorption at 765 cm^{-1}. The inset expands the $Mn^{III}Mn^{IV}$ absorption at 700 cm^{-1}.

Figure 7: (I) FT-Raman spectra of Cr-AlMCM-41 grafted with 1.5 wt% $(bpy)_2Mn^{III}(\mu\text{-}O)_2Mn^{IV}(bpy)_2$ which was illuminated with a 458 nm laser operating at 170 mW. (A) Before illumination, (B) illumination for 5 minutes, (C) for 30 minutes. Spectrum (D) is 0.5 wt% $(bpy)_2Mn^{III}(\mu\text{-}O)_2Mn^{IV}(bpy)_2$ loaded in AlMCM-41. (II) The same photolysis experiment conducted with 1.5 wt% $(bpy)_2Mn^{III}(\mu\text{-}O)_2Mn^{IV}(bpy)_2$ loaded onto AlMCM-41. (E) Before illumination, (F) illumination for 5 minutes, ((G) for 30 minutes. *Denotes residual acetonitrile. Growth of a band at 805 cm^{-1} upon illumination is noted in spectra (I)A, B, and C; assignment to $\nu(Cr^{V}\text{-}O)$ is uncertain because of overlap with the silica absorption around 800 cm^{-1}.

Figure 8: X-band EPR spectra of $(bpy)_2Mn^{III}(\mu\text{-}O)_2Mn^{IV}(bpy)_2$ (1.5 wt%) on Cr-AlMCM-41 and AlMCM-41 illuminated at 458 nm. (A) Before, (B) after 30 minutes illumination of complex in Cr-AlMCM-41. (C) Before, (D) after 30 minutes illumination of complex in AlMCM-41. Spectra are from

the same samples whose FT-Raman spectra are shown in figure 6, traces A,C,E, and G, respectively. Spectra are normalized per mg of material.

Figure 9: Mn(I) and Cr(II) K-edge XANES of $(bpy)_2Mn^{III}(\mu\text{-}O)_2Mn^{IV}(bpy)_2$ (1.5 wt%) on Cr-AlMCM-41 before (trace A) and after (trace B) illumination with a 458 nm laser emission for 30 minutes.

Table 1

Fit	Sample – Figure #	Shell	R (Å)	N (with S_0^2=0.85)	σ^2(Å^2)x10^3	Φ(x10^3)	ε^2(x10^5)
1	Pure – 1A	Mn-O Mn-N	1.78 2.10	0.9 2.3	1 13	0.4	0.16
2	Mn_2 on AlMCM – 1B	Mn-O Mn-N	1.81 2.15	1.2 2.2	1.6 12	0.3	0.12
3	Mn_2 on CrAlMCM – 1C	Mn-O Mn-N	1.80 2.08	1.1 2.7	0.8 25	0.8	0.37
4	Pure – 1A	Mn-Mn	2.73	0.6	2*	0.6	0.28
5	Mn_2 on AlMCM – 1B	Mn-Mn	2.72	0.5	2*	0.4	0.19
6	Mn_2 on CrAlMCM – 1C	Mn-Mn	2.74	0.5	2*	0.6	0.28

Table 2

Fit	Sample – Figure #	Shell	R (Å)	N (with S_0^2=1.0)	σ^2(Å^2)x10^3	Φ(x10^3)	ε^2(x10^5)
1	CrAlMCM – 4A	Cr-O	1.64	2.2	2*	1.3	0.69
2	Mn_2 on CrAlMCM – 4C	Cr-O	1.64	1.7	2*	0.9	0.47
3	Mn_2 max CrAlMCM – 4B	Cr-O	1.65	2.1	2*	0.7	0.38
4	CrAlMCM – 4A	Cr-O Cr-O	1.64 1.87	2.8 1.1	2*	0.8	0.44
5	Mn_2 on CrAlMCM – 4C	Cr-O Cr-O	1.65 1.91	2.0 0.6	2*	0.6	0.34
6	Mn_2 max CrAlMCM – 4B	Cr-O Cr-O	1.65 1.89	2.3 0.5	2*	0.6	0.32

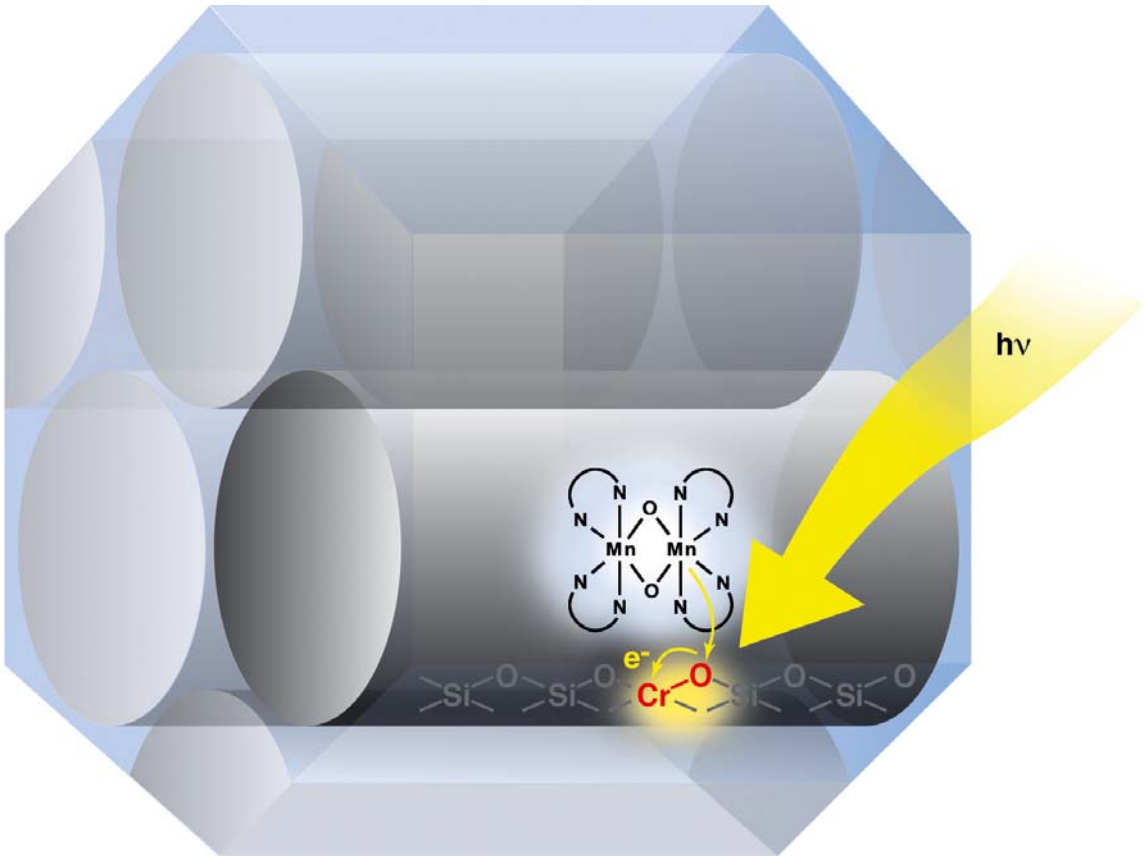

Figure 1: A schematic representation of the photon-induced electron transfer reaction. Light excites a Cr^{VI}-O LMCT, creating the high energy intermediate that transfers an electron from $(bpy)_2Mn^{III}(\mu\text{-}O)_2Mn^{IV}(bpy)_2$ into Cr^{VI}, generating a Cr^{V}.

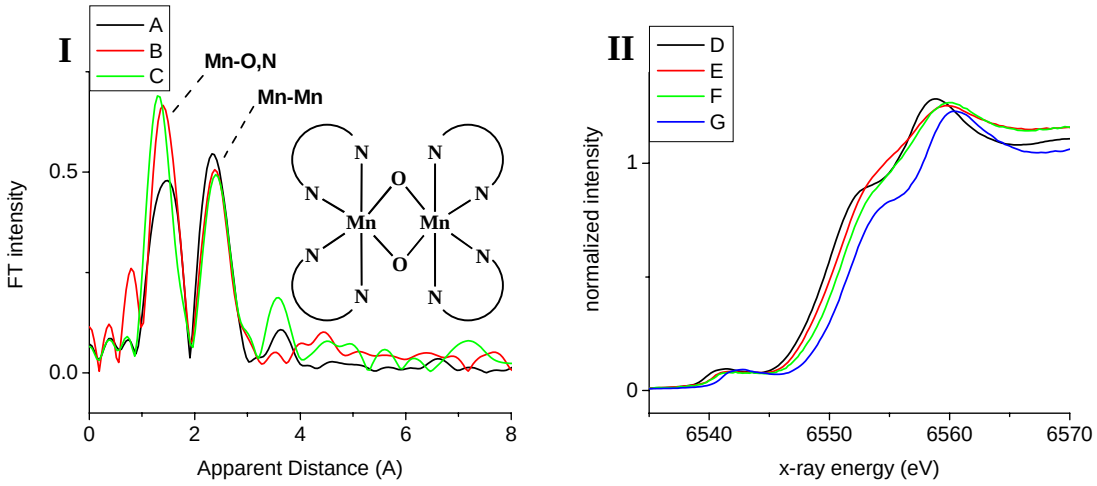

Figure 2: (I) FT of the k^3-weighted Mn K-edge EXAFS of (A) crystalline $[(bpy)_2Mn^{III}(\mu\text{-}O)_2Mn^{IV}(bpy)_2](NO_3)_3$. (B) $(bpy)_2Mn^{III}(\mu\text{-}O)_2Mn^{IV}(bpy)_2$ loaded (0.5 wt%) into AlMCM-41. (C) Complex loaded into Cr-AlMCM-41 (Cr/Si = 0.01). (II) Mn K-edge XANES of (D) crystalline $[(bpy)_2Mn^{III}(\mu\text{-}O)_2Mn^{IV}(bpy)_2](NO_3)_3$. $(bpy)_2Mn^{III}(\mu\text{-}O)_2Mn^{IV}(bpy)_2$ loaded into (E) AlMCM-41 (0.5 wt%), (F) complex loaded into Cr-AlMCM-41. (G) Crystalline $[(Me_2\text{-}bpy)_2Mn^{IV}(\mu\text{-}O)_2Mn^{IV}(Me_2\text{-}bpy)_2][ClO_4]_4$. D and G are included to reference the edge position of $Mn_2^{III/IV}$ and $Mn_2^{IV/IV}$, respectively.

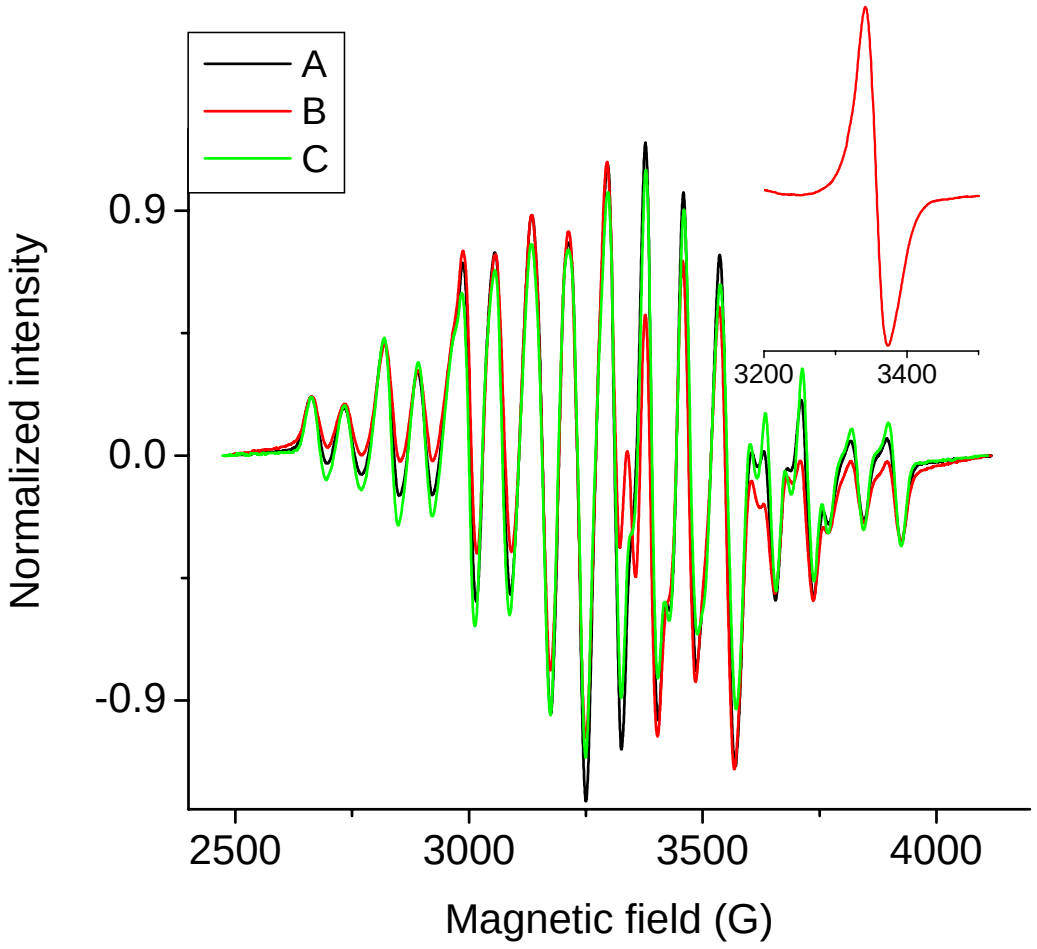

Figure 3: X-band EPR spectra of $(bpy)_2Mn^{III}(\mu\text{-}O)_2Mn^{IV}(bpy)_2$ grafted into (A) AlMCM-41, (B) Cr-AlMCM-41. (C) $[(bpy)_2Mn^{III}(\mu\text{-}O)_2Mn^{IV}(bpy)_2](NO_3)_3$ in acetonitrile solution. Spectra were recorded at 20 K. The small signal at ~3300 G originates from the residual Cr^{V} present in Cr-AlMCM-41. Inset is an EPR spectrum of calcined Cr-AlMCM-41 for comparison.

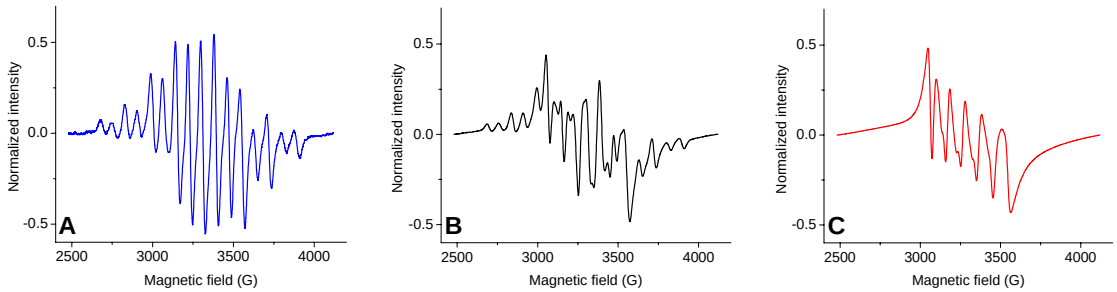

Figure 4: X-band EPR signal of AlMCM-41 grafted with 4 wt% $terpy_2Mn_2O_2$. The samples were kept under ambient conditions for (A) 10 minutes, (B) 6 hours, and (C) 7 days after grafting was complete, then frozen under liquid N_2 for EPR analysis. EPR intensities were arbitrarily normalized for comparison.

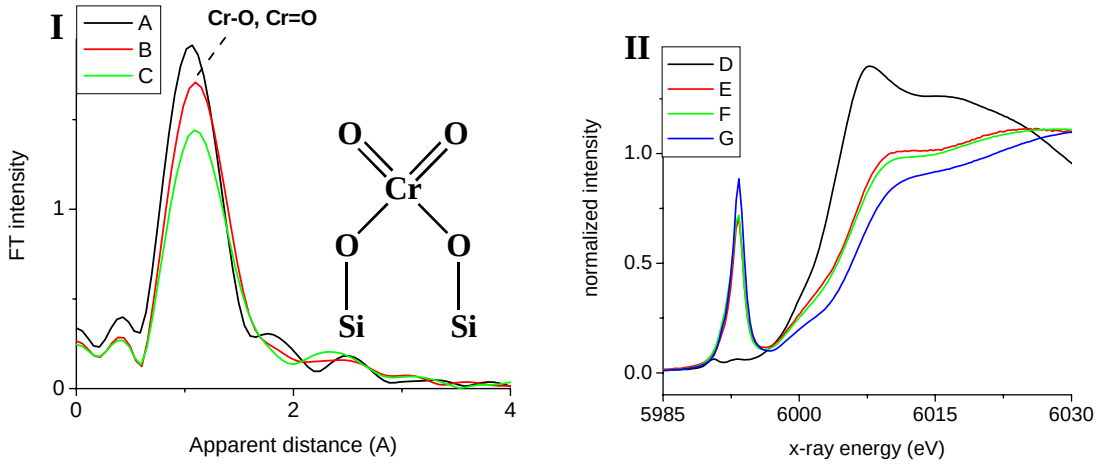

Figure 5: (I) FT of k^3-weighted Cr K-Edge EXAFS of (A) Cr-AlMCM-41, (B) Cr-AlMCM-41 grafted with 9.5 wt% $(bpy)_2Mn^{III}(\mu\text{-}O)_2Mn^{IV}(bpy)_2$, (C) Cr-AlMCM-41 grafted with 0.5 wt% $(bpy)_2Mn^{III}(\mu\text{-}O)_2Mn^{IV}(bpy)_2$. (II) Cr K-edge XANES of (D) $Cr(NO_3)_3$ (solid Cr(III) compound), (E) Cr-AlMCM-41 treated with 0.01 M 4,4'-bipyridine, (F) Cr-AlMCM-41 grafted with 0.5 wt% $(bpy)_2Mn^{III}(\mu\text{-}O)_2Mn^{IV}(bpy)_2$, (G) calcined Cr-AlMCM-41.

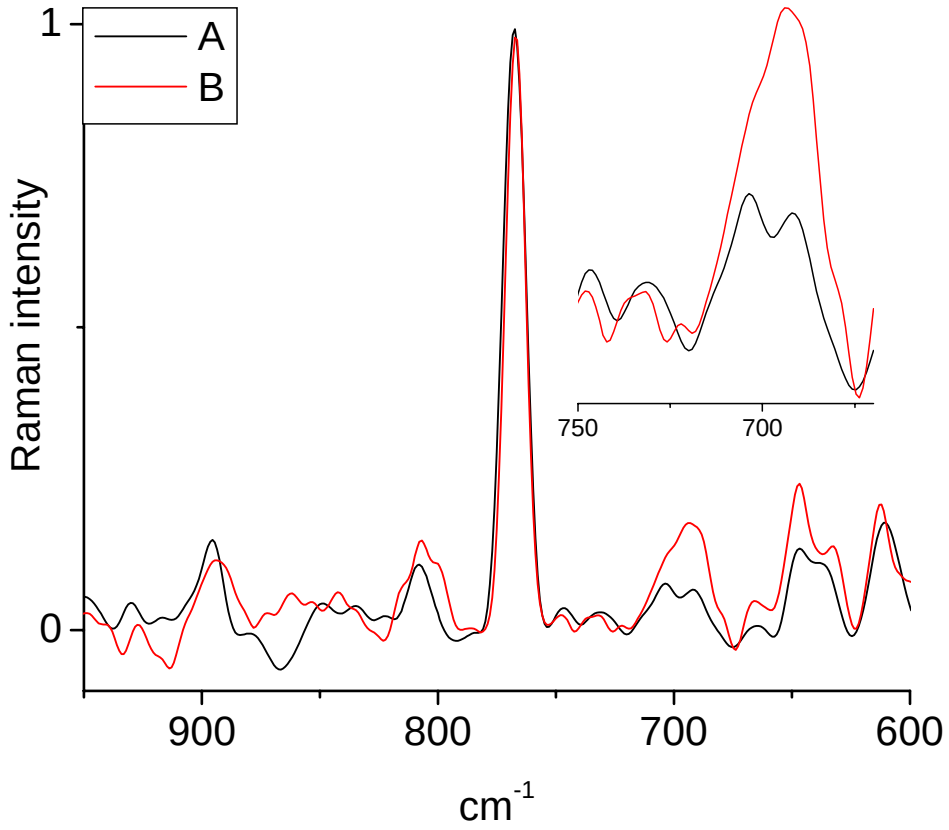

Figure 6: FT-Raman of $(bpy)_2Mn^{III}(\mu\text{-}O)_2Mn^{IV}(bpy)_2$ grafted onto Cr-AlMCM-41 in different weight ratios: (A) 2.5 wt%, (B) 5.0 wt%. Spectra are normalized relative to the bipyridyl ligand absorption at 765 cm^{-1}. The inset expands the $Mn^{III}Mn^{IV}$ absorption at 700 cm^{-1}.

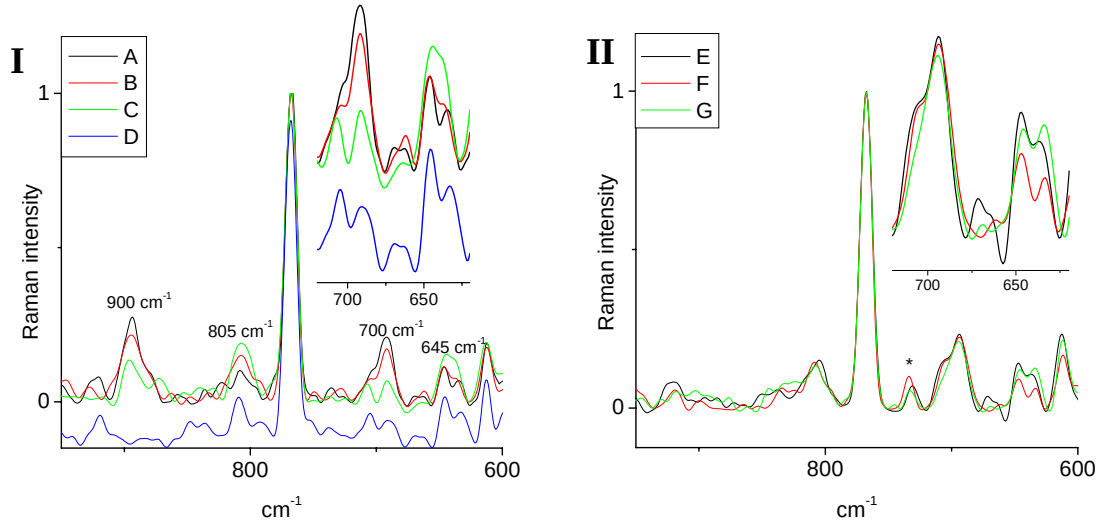

Figure 7: (I) FT-Raman spectra of Cr-AlMCM-41 grafted with 1.5 wt% $(bpy)_2Mn^{III}(\mu\text{-}O)_2Mn^{IV}(bpy)_2$ which was illuminated with a 458 nm laser operating at 170 mW. (A) Before illumination, (B) illumination for 5 minutes, (C) for 30 minutes. Spectrum (D) is 0.5 wt% $(bpy)_2Mn^{III}(\mu\text{-}O)_2Mn^{IV}(bpy)_2$ loaded in AlMCM-41. (II) The same photolysis experiment conducted with 1.5 wt% $(bpy)_2Mn^{III}(\mu\text{-}O)_2Mn^{IV}(bpy)_2$ loaded onto AlMCM-41. (E) Before illumination, (F) illumination for 5 minutes, ((G) for 30 minutes. *Denotes residual acetonitrile. Growth of a band at 805 cm^{-1} upon illumination is noted in spectra (I)A, B, and C; assignment to $\nu(Cr^{V}\text{-}O)$ is uncertain because of overlap with the silica absorption around 800 cm^{-1}.

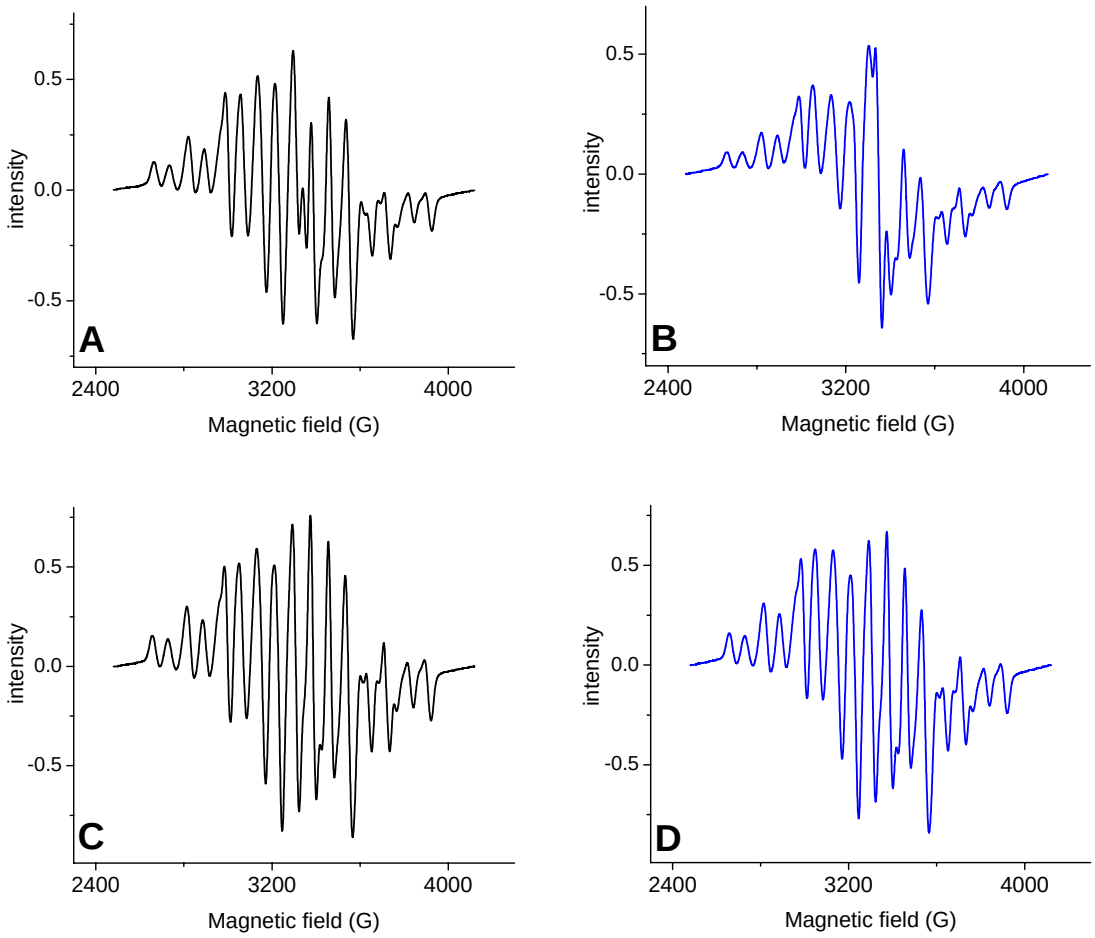

Figure 8: X-band EPR spectra of $(bpy)_2Mn^{III}(\mu\text{-}O)_2Mn^{IV}(bpy)_2$ (1.5 wt%) on Cr-AlMCM-41 and AlMCM-41 illuminated at 458 nm. (A) Before, (B) after 30 minutes illumination of complex in Cr-AlMCM-41. (C) Before, (D) after 30 minutes illumination of complex in AlMCM-41. Spectra are from the same samples whose FT-Raman spectra are shown in figure 6, traces A,C,E, and G, respectively. Spectra are normalized per mg of material.

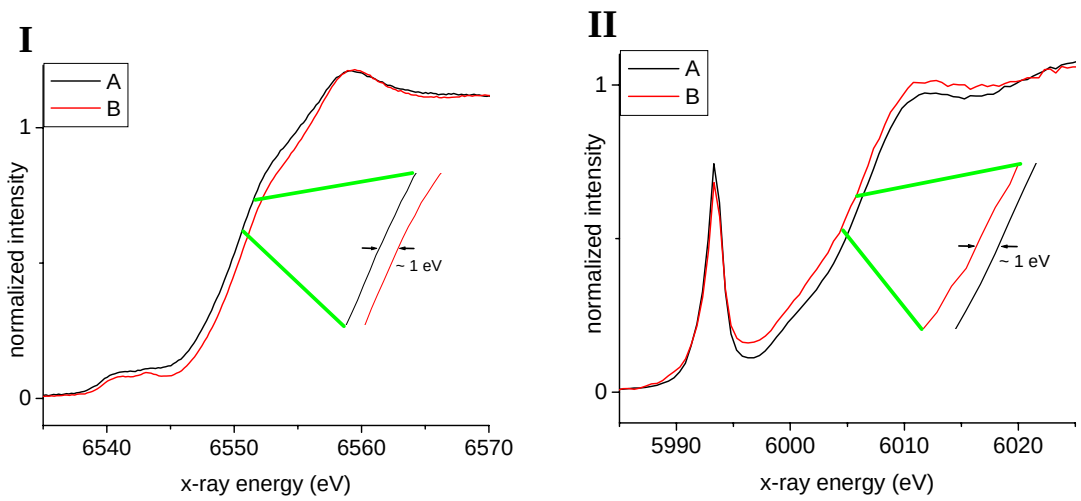

Figure 9: Mn(I) and Cr(II) K-edge XANES of $(bpy)_2Mn^{III}(\mu\text{-}O)_2Mn^{IV}(bpy)_2$ (1.5 wt%) on Cr-AlMCM-41 before (trace A) and after (trace B) illumination with a 458 nm laser emission for 30 minutes.